

Mapping the elastic properties of granular Au films by contact resonance atomic force microscopy

G Stan and R F Cook

Ceramics Division, National Institute of Standards and Technology, Gaithersburg, MD 20899, USA

E-mail: gheorghe.stan@nist.gov

Received 21 February 2008, in final form 24 March 2008

Published 7 May 2008

Online at stacks.iop.org/Nano/19/235701

Abstract

Endowed with nanoscale spatial resolution, contact resonance atomic force microscopy (CR-AFM) provides extremely localized elastic property measurements. We advance here the applicability of CR-AFM on surfaces with nanosize features by considering the topography contribution to the CR-AFM signal. On nanosize granular Au films, the elastic modulus at the grain scale has been mapped out by considering a self-consistent deconvolution of the contact geometry effect in the CR-AFM image. Significant variation in the contact area over granular topography arises as the probe is either in single- or multiple-asperity contact with the surface. Consequently, in extracting the elastic modulus from CR-AFM measurements on granular surfaces we considered both the normal and lateral couplings established through multiple-asperity contacts between the tip and the surface. Thus, by appropriately considering the change in the contact mechanics during CR-AFM imaging, variations in the elastic modulus have been revealed in the intergrain regions as well as across individual grains.

(Some figures in this article are in colour only in the electronic version)

1. Introduction

Next-generation electronic devices, based on micro- and nanoelectromechanical systems (MEMS and NEMS) [1], require accurate knowledge and control of material properties at ultra-small scales. As the size of device elements is reduced further and further, down to the nanoscale, mechanical properties in particular can exhibit significant variations from those of their bulk counterparts due to the increase in the surface-to-volume ratio. The inherent effects of proximate surfaces and interfaces alter the properties of the nanosize entities (e.g., nanotubes [2], nanowires [3], nanoparticles [4]) or those of reduced-scale constituents (e.g., crystallites in nanostructured materials [5]) and modify the mechanical response of the assembly as a whole. For some particular geometries it is possible to deduce the response of the nanosized constituents by testing an assembly at the macroscale [6]. However, it is obviously more desirable to directly probe the local mechanical properties of a nanostructured material [7–10].

Instrumentation developed for nanoscale characterization, such as atomic force microscopy (AFM), enables access at ultra-small scales but brings the challenge of extracting and quantifying material properties from measurements made with such instruments. It is also desirable to make non-destructive and *in situ* characterization of elements of nanostructured assemblies. These needs can be addressed by expanding the capabilities of AFM techniques to provide local property measurements based on accurate knowledge of the interaction between the testing probe and the investigated structure. Endowed with high spatial resolution and accurate force control, techniques such as contact resonance AFM (CR-AFM) (which includes atomic force acoustic microscopy (AFAM) [11] and ultrasonic atomic force microscopy [12]) and other AFM related techniques (ultrasonic force microscopy (UFM) [13], heterodyne force microscopy [14], passive overtone microscopy [15], resonant difference-frequency atomic force ultrasonic microscopy [16]) have been used to quantify the elastic properties of the probe–sample contact. By taking advantage of the in-plane scanning capability of

AFM, CR-AFM measurements made at each point in the scan produced maps of the elastic modulus with nanoscale spatial resolution [17–21].

In this work we used CR-AFM to map, with spatial resolution better than 10 nm, the elastic modulus of granular Au thin films. By measuring the contact resonance frequency of a vibrated AFM probe in contact with the investigated film, the contact stiffness was determined at every point in the CR-AFM scan. The contact geometry was subsequently resolved based on the local topography acquired by scanning tunneling microscopy (STM). With a self-consistent deconvolution of contact geometry effects in the CR-AFM image, an elastic modulus map was then generated. In contrast to the usual CR-AFM measurements on flat surfaces, the contact geometry on granular surfaces is complicated by the possible formation of multiple-asperity contacts between the tip and nearby contacted grains. In extracting the elastic modulus from CR-AFM measurements on granular surfaces we considered both the normal and lateral couplings established through multiple-asperity contacts between the tip and the surface. The acknowledged change in the contact area due to these local contact couplings has been accurately correlated with the measured contact resonance frequency at every point in the scan. As a result, variations in the elastic modulus have been revealed in the intergrain regions as well as across individual grains. In much the same way, correlations between topography and contact resonance images need to be resolved together for CR-AFM mapping of elastic modulus at the nanoscale.

2. Theoretical background

As in any other contact mode AFM-based techniques, in CR-AFM the sample is probed by bringing the AFM sensor tip in contact with the sample surface. A small-amplitude mechanical vibration with frequency in the kilohertz to megahertz range is then superposed on the loaded AFM cantilever. This vibration is transmitted through the AFM tip and excites acoustic waves in the sample. The cantilever's end conditions are modified by the tip–sample coupling and this change is directly observed in the resonance frequency of the vibrated cantilever. Thus, in CR-AFM, both the mechanics of the tip–sample contact and the dynamics of the clamped-coupled cantilever are important in extracting the local material property of the sample tested. A detailed theoretical and experimental review of a vibrated AFM probe in contact with materials can be found in [22]. In this section we will describe the contact mechanics occurring when an AFM probe contacts a sample surface through either a single-asperity contact (SAC) or a multiple-asperity contact (MAC). The effect on cantilever dynamics due to a change in contact area in SAC and MAC will be then analyzed.

In CR-AFM, the load applied to the tip–sample contact is chosen to be large enough to exceed adhesion contact forces but small enough to prevent plastic deformation at the contact. Under these restrictions, the contact is deformed elastically and the simple model of such elastic tip–sample coupling is that of a linear spring. The idealized system, schematically shown in

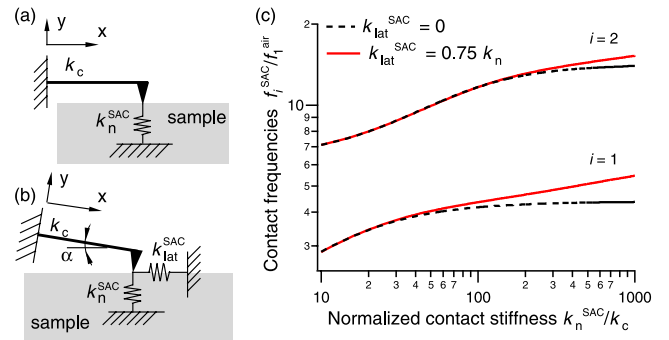


Figure 1. Idealized AFM probe (cantilever and tip) spring-coupled through a SAC to the surface: (a) only normal contact coupling is considered, (b) both normal and lateral contact couplings are considered; (c) the effect of the lateral contact coupling on the first two ($i = 1, 2$) contact resonance frequencies of the cantilever as a function of the normal contact stiffness in SAC. The frequencies are normalized to the first resonance frequency of the cantilever in air, f_1^{air} .

figure 1(a), consists of a beam clamped at one end and spring-coupled at the other [11].

For a SAC between the spherical end of the tip and a flat surface, the normal contact stiffness, k_n^{SAC} , characterizing the elastic deformation of the contact along the direction normal to the surface, is given by the derivative of the normal force, F_n , with respect to the approach distance, δ_n , between the two bodies in contact. In the Hertz contact model [23], k_n^{SAC} is expressed as:

$$k_n^{\text{SAC}} = \frac{\partial F_n}{\partial \delta_n} = 2\sqrt{A_c^{\text{SAC}}/\pi E^*}. \quad (1)$$

The SAC contact area is $A_c^{\text{SAC}} = \pi a^2$, with the contact radius given by

$$a = \left(\frac{3F_n R_T}{4E^*} \right)^{1/3}. \quad (2)$$

Here, R_T is the radius of the tip and E^* is the reduced elastic modulus given by the indentation moduli of the tip, M_T , and the sample, M_S :

$$1/E^* = 1/M_T + 1/M_S. \quad (3)$$

For elastically isotropic materials the indentation modulus is simply expressed in terms of the Young's modulus E and the Poisson's ratio ν , $M = E/(1 - \nu^2)$. In the general case of elastically anisotropic materials, the indentation modulus can be numerically calculated along the indentation direction as a function of the elastic constants of the indented material [24].

Another spring-coupling that contributes to the dynamics of the system is that of the lateral contact stiffness (see figure 1(b)). This is caused by the mechanical vibrations that are induced in the surface plane of the sample. Two things contribute to this: one is the tilt of the cantilever with respect to the sample's surface and the other is the rocking of the tip in the cantilever–tip plane caused by the flexural waves that vibrate the cantilever. The lateral contact stiffness for a single-asperity Hertzian contact is defined as the change in

the tangential contact force F_{lat} with the lateral displacement δ_{lat} [25]:

$$k_{\text{lat}}^{\text{SAC}} = \partial F_{\text{lat}} / \partial \delta_{\text{lat}} = 8\sqrt{A_c^{\text{SAC}} / \pi G^*}, \quad (4)$$

with A_c^{SAC} the SAC contact area defined above and G^* the reduced shear modulus of the tip and the sample. If the tip and the sample are isotropic materials, then G^* is given by

$$1/G^* = (2 - \nu_T)/G_T + (2 - \nu_S)/G_S, \quad (5)$$

where G_T and ν_T are shear modulus and Poisson's ratio for the tip, and G_S and ν_S are shear modulus and Poisson's ratio for the sample. In the anisotropic case, similar to the normal indentation modulus M , a shear indentation modulus, N , would appropriately describe the lateral deformation of the tip-sample contact; in the isotropic case, $N = G/(2 - \nu)$ [26]. Roughly, if $E_T \gg E_S$, $k_{\text{lat}}^{\text{SAC}}/k_n^{\text{SAC}} \approx 2(1 - \nu_S)/(2 - \nu_S)$ [27]. For exemplification we will use in the following an average value 0.40 for the Poisson's ratio of Au, which gives 0.75 for the ratio $k_{\text{lat}}^{\text{SAC}}/k_n^{\text{SAC}}$.

We now analyze how the cantilever dynamics is affected by these two springs, normal and lateral, coupled at the unclamped end of the cantilever. To do that, the wave equation for the flexural vibrations in the cantilever beam [28],

$$EI \frac{\partial^4 y(x, t)}{\partial x^4} + \rho A \frac{\partial^2 y(x, t)}{\partial t^2} = 0, \quad (6)$$

is solved for the geometry shown in figure 1(b). Here, E is the Young's modulus along the long axis of cantilever, I is the moment of inertia of the cross section of the cantilever, ρ is the density, and A is the cross sectional area of the cantilever. The cantilever's stiffness is given by $k_c = 3EI/L^3$, where L is the length of the cantilever. The coordinate system is chosen with the x and y axes directed along the cantilever's length axis and perpendicular to it, respectively, and t is time. For the system shown in figure 1(b), the solution of (6),

$$y(x, t) = [A_1(\cos kx + \cosh kx) + A_2(\cos kx - \cosh kx) + A_3(\sin kx + \sinh kx) + A_4(\sin kx - \sinh kx)]e^{i\omega t}, \quad (7)$$

with A_1 , A_2 , A_3 , and A_4 constants, has to satisfy the following boundary conditions at the fixed (clamped) end, $x = 0$, and at the spring-coupled end, $x = L$, of the cantilever: [29]

$$y(x, t)|_{x=0} = 0, \quad (8)$$

$$\left. \frac{\partial y(x, t)}{\partial x} \right|_{x=0} = 0, \quad (9)$$

$$EI \left. \frac{\partial^2 y(x, t)}{\partial x^2} \right|_{x=L} = -F_x h, \quad (10)$$

$$EI \left. \frac{\partial^3 y(x, t)}{\partial x^3} \right|_{x=L} = F_y \quad (11)$$

with

$$F_x = h(k_n^{\text{SAC}} \sin^2 \alpha + k_{\text{lat}}^{\text{SAC}} \cos^2 \alpha) \left. \frac{\partial y(x, t)}{\partial x} \right|_{x=L} + \sin \alpha \cos \alpha (k_{\text{lat}}^{\text{SAC}} - k_n^{\text{SAC}}) y(x, t)|_{x=L} \quad (12)$$

and

$$F_y = h \sin \alpha \cos \alpha (k_{\text{lat}}^{\text{SAC}} - k_n^{\text{SAC}}) \left. \frac{\partial y(x, t)}{\partial x} \right|_{x=L} + (k_n^{\text{SAC}} \cos^2 \alpha + k_{\text{lat}}^{\text{SAC}} \sin^2 \alpha) y(x, t)|_{x=L}. \quad (13)$$

Here, k is the flexural wavenumber; h is the height of the AFM tip; α is the tilt angle of the cantilever with respect to the sample's surface; and $\omega = k^2 \sqrt{EI/\rho A}$ is the angular frequency of the flexural cantilever vibrations. The characteristic equation obtained from the above equations provides the dispersion relationship for the resonance frequencies of the clamped-coupled cantilever as a function of the contact spring-coupling stiffnesses [22]:

$$\begin{aligned} & \gamma^4(1 + \cos \gamma \cosh \gamma) \\ & + \gamma^3(\sin \gamma \cosh \gamma + \cos \gamma \sinh \gamma) C_1 \\ & + 2\gamma^2 \sin \gamma \sinh \gamma C_2 \\ & + \gamma(\sin \gamma \cosh \gamma - \cos \gamma \sinh \gamma) C_3 \\ & + (1 - \cos \gamma \cosh \gamma)(C_1 C_3 - C_2^2) = 0 \end{aligned} \quad (14)$$

with $\gamma = kL$, $C_1 = 3(h/L)^2(k_n \sin^2 \alpha + k_{\text{lat}} \cos^2 \alpha)/k_c$, $C_2 = 3(h/L) \sin \alpha \cos \alpha (k_{\text{lat}} - k_n)/k_c$, and $C_3 = 3(k_n \cos^2 \alpha + k_{\text{lat}} \sin^2 \alpha)/k_c$. A more general treatment of this problem can be found in [22].

In figure 1(c) are shown the first two resonance frequencies of the clamped-coupled cantilever as a function of the normal contact stiffness for two cases: when the lateral contact coupling is neglected as in figure 1(a) and when $k_{\text{lat}}^{\text{SAC}} = 0.75k_n^{\text{SAC}}$ as in figure 1(b). The cantilever tilt angle was $\alpha = 11^\circ$ (as specified by the manufacturer of the AFM used in this work) and the ratio $h/L = 0.06$ (as calculated with the tip parameters specified in section 3). As can be seen, the contact resonance frequencies experience larger and larger increases as the normal contact coupling becomes stiffer and stiffer. For the range of normal contact stiffness shown here, the first contact resonance frequency is more sensitive to lateral coupling than the second. This is because in the first vibrational mode the angular cantilever deflections at the tip position are larger than in the second mode. (We exploited this observation and used the first contact resonance mode for imaging in our experiments; with a small applied load, the normal contact stiffness was restricted to values below $100 k_c$.) We now analyze the effect on cantilever dynamics due to the increase in the contact area in a MAC, the case that has to be considered when CR-AFM is used for imaging nanoscale featured topographies.

The contact area maintained between an AFM tip and the investigated surface during contact-AFM scanning is continuously modulated by the nanoscale roughness of the surface. When the wavelength of the summits intercepted by the tip is large or very small compared to the contact radius, the contact formed is nominally a SAC. In this case the size of the contact area varies around an average value characterizing the contact between the tip and an ideally flat surface. However, on surfaces with roughness of wavelength and amplitude comparable with the tip radius (e.g., granular surfaces studied in this work), the contact not only varies in size due to the small-wavelength roughness but also due to

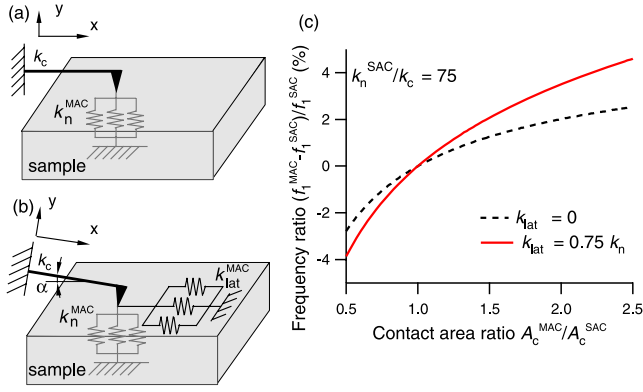


Figure 2. Schematics of the AFM cantilever with (a) normal contact spring-coupling and (b) with normal and lateral contact spring-couplings in MAC. (c) The relative variation of the contact resonance frequency as a function of the ratio of the contact areas in MAC and SAC.

the number of contacts. Thus, on such granular surfaces, the contact is a SAC on top of the grains whereas between grains the probe could be simultaneously in contact with two or three grains and form a MAC. Considering the grains as spherical summits of radius of curvature $R_S^{(i)}$, the contact area at a given location is obtained as a summation over the Hertzian-elastically deformed grains that contact the probe at that location [23]:

$$A_c^{\text{MAC}} = \sum_i \pi a_i^2 = \pi \sum_i \delta_i R_i. \quad (15)$$

Here, δ_i is the depth of deformation between the tip and summit i , with $1/R_i = 1/R_T + 1/R_S^{(i)}$ the relative curvature at the contact. In the case of MAC, the applied load is distributed between the summits that are in contact with the tip

$$P = \frac{4}{3} \sum_i E_i^* R_i^{1/2} \delta_i^{3/2} \approx \frac{4}{3} \langle E^* \rangle \sum_i R_i^{1/2} \delta_i^{3/2}. \quad (16)$$

In (16), $\langle E^* \rangle$ defines the local average of the reduced elastic modulus at the MAC and describes the equivalent elastic response of the summits forming the contact.

The normal contact stiffness of a MAC is then the equivalent stiffness of the parallel-coupled summits, schematically shown in figure 2(a):

$$k_n^{\text{MAC}} = 2\sqrt{A_c^{\text{MAC}}/\pi} \langle E^* \rangle, \quad (17)$$

with A_c^{MAC} defined in (15). Similar to (4), the lateral contact stiffness is defined as:

$$k_{\text{lat}}^{\text{MAC}} = 8\sqrt{A_c^{\text{MAC}}/\pi} \langle G^* \rangle, \quad (18)$$

with $\langle G^* \rangle$ the local average of the reduced shear modulus of MAC between the tip and the contacted grains. A schematic diagram of the lateral coupling in MAC is shown in figure 2(b).

The effect of contact area variation in a MAC on the resonance frequency of the first vibrational mode of the cantilever is shown in figure 2(c). As the measured

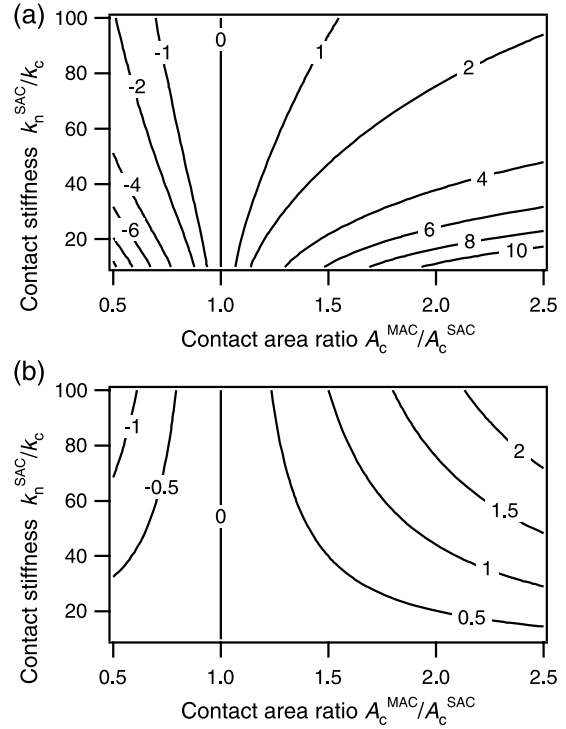


Figure 3. (a) The variation $(f_1^{\text{MAC}} - f_1^{\text{SAC}})/f_1^{\text{SAC}}$ of the first contact resonance frequency as a function of the normalized contact stiffness and the ratio of contact areas in MAC and SAC; no lateral coupling was considered. (b) The additional increase to the first contact resonance frequency plotted in (a) when a lateral coupling $k_{\text{lat}}/k_n = 0.75$ is further considered. The contours are calculated in per cents.

relative contact stiffness, k_n^{SAC}/k_c , on the granular Au films investigated in section 3 is in the 40–100 range, we chose for the discussion here a value of 75 for this parameter. Thus, in figure 2(c), the relative change in the resonance frequency in MAC is compared to SAC as a function of the ratio of MAC and SAC areas (the SAC area is considered constant in this analysis). As an example, if the contact area doubles due to multiple contacts, the increase in the normal contact stiffness will determine an enhancement of about 2% in the first resonance frequency compared with SAC. A larger increase in the resonance frequency results in the case of a MAC with lateral coupling: about 4% for the same increase in the contact area. This shows that the change in the contact area affects the resonance frequency of the cantilever through both normal and lateral contact spring-couplings. Such an effect, of the contact resonance frequency shifting towards greater values, can be observed also in SAC when the increase in the contact area is due to tip wear [30].

Furthermore, we have analyzed the effect of contact area variation on the contact resonance frequency for an extended range of contact stiffness values. As above, the analysis was carried out for the cases with only normal contact coupling and with both normal and lateral contact couplings. Thus, the relative change of the first contact resonance frequency, $(f_1^{\text{MAC}} - f_1^{\text{SAC}})/f_1^{\text{SAC}}$, due to the increase of the contact area of a MAC, is shown in figure 3(a) as contours in the plane

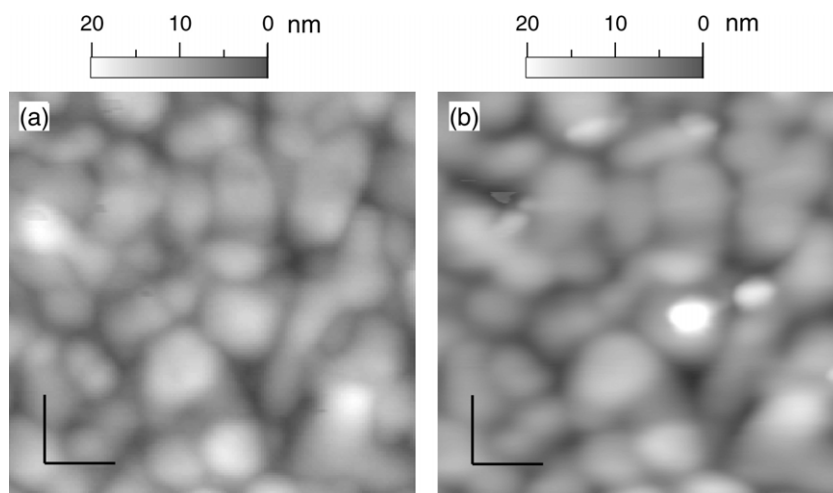


Figure 5. AFM topography of the Au film (a) before CR-AFM and (b) after CR-AFM. The scale bars are 100 nm.

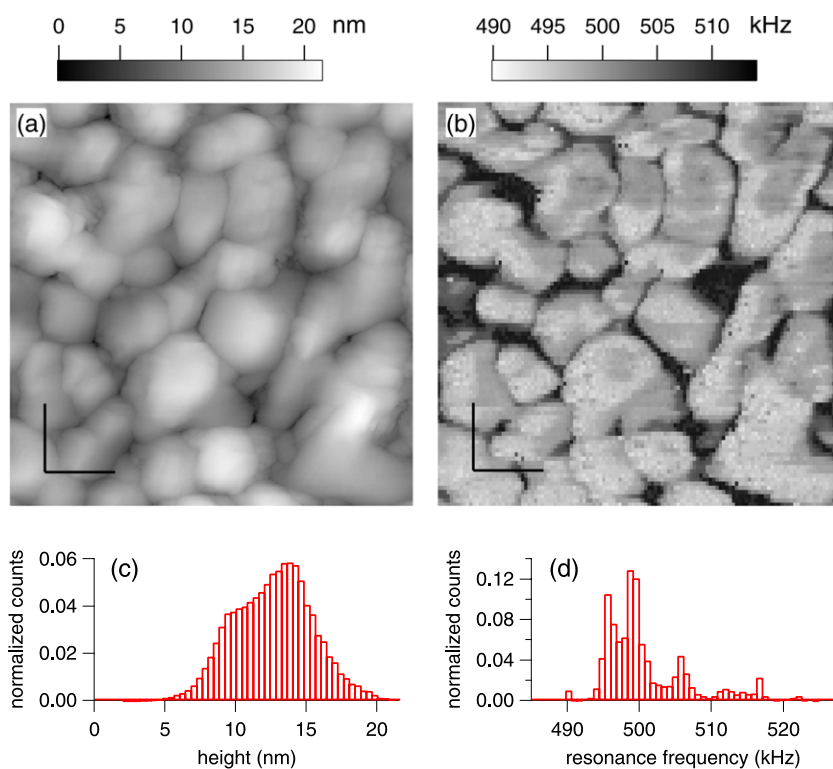


Figure 6. (a) STM and (b) CR-AFM mapping of the first contact resonance over the area shown in (a) and figure 5. The scale bars are 100 nm. The normalized histograms in (c) and (d) were constructed from the quantities mapped in (a) and (b).

topographical information from the STM image made over the investigated area. Thus, after AFM and CR-AFM scans, the investigated area has been imaged with STM by using the STM head of the same microscope. The STM scan was made in air with a Pt/Ir tip (PT-ECM Digital Instruments, Santa Barbara, CA) (see footnote 1). As can be seen in the STM image (figure 6(a)), the grains appeared unaffected as the result of the successive scans. The STM image rather than the AFM images will be used later to perform the contact geometry reconstruction that is needed in calculating the elastic modulus map. The reason is that, as is known, the AFM

image results from a convolution between the real surface topography and the tip used in scanning. So, in order to use the AFM image as real surface topography, a preliminary tip-surface deconvolution is required, in which case many topographical features (observed in great detail in the STM image) are difficult to recover. On the other hand, in the nanoscale to microscale range (as is the case of the granular Au films investigated here) a more realistic surface topography is provided by the constant-current STM image as at this scale the current density does not vary significantly on metallic surfaces. The histograms in figures 6(c) and (d) show very

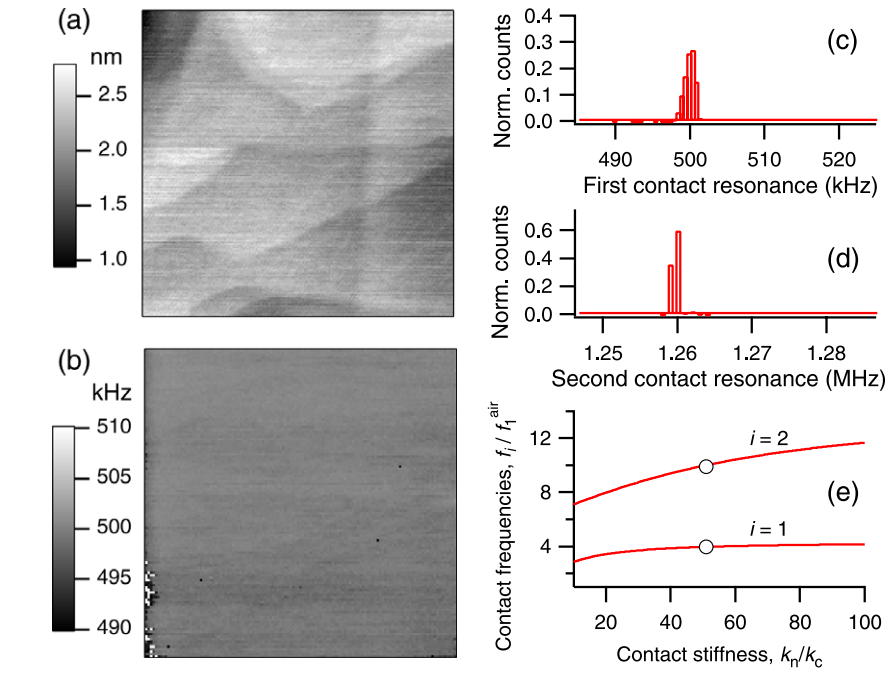


Figure 7. CR-AFM measurements on Au(111) reference material: (a) AFM topography over $1 \mu\text{m}^2$ area of the Au reference film; (b) the map of the first contact resonance frequency over the area shown in (a); (c) and (d) histograms of the first contact resonance frequency (shown in (b)) and the second resonance frequency from CR-AFM image over the area shown in (a); (e) contact resonance frequencies versus contact stiffness: measurements for Au(111) reference and theoretical curves from the clamped-coupled beam model [11].

clearly that large variations occur in both topography and CR-AFM scans. Consequently, the change in the contact area has to be considered in calculating the elastic modulus from CR-AFM measurements.

Nominally, a slightly reduction in the elastic modulus is expected to occur in the intergrain regions as a result of the orientation mismatch between adjacent grains [32]. Contrarily, in the intergrain regions in figure 6(b), the contact resonance frequency is observed to increase. This is because, when the tip radius is comparable in size with the local radius of curvature of the surface, besides the modulation in the elastic modulus due to material properties, the CR-AFM measurements are also sensitive to the topographical features that modify the contact area. In some previous works on mapping the elastic response of materials at the nanoscale, by either AFAM [19, 21] or UFM [33], the topographic artifacts [8, 34] in the elastic image were negligible on surfaces with radii of curvature much larger than the tip radius. In the next section, by correlating the STM and CR-AFM images, we will consider the variations in the contact area due to non-flat topography and correct the CR-AFM elastic map for these variations.

In terms of the absolute value of the elastic modulus, we have compared the measurements with those made on a Au(111) reference material under the same experimental conditions [20, 30]. The reference was a 300 nm thick Au(111) film epitaxially grown on mica (Georg Albert PVD-Beschichtungen, Heidelberg, Germany) (see footnote 1). As can be seen in figure 7(a) the surface of the Au reference film is essentially flat over large areas, with a rms roughness of 0.2 nm over $1 \mu\text{m}^2$. In this case, because there are minor changes in the contact area, the most probable contact

resonance frequencies were precisely determined by fitting the histograms of the measurements shown in figures 7(c) and (d) [20], with Gaussian distributions. By using a beam-cantilever model [11], the relative stiffness of the contact along the tip axis was calculated as $k_n^{\text{SAC}}/k_c = 50.9$ on Au(111) reference as is shown in figure 7(e). Considering that the Au(111) reference material is characterized by an indentation modulus $M_{\text{Au}(111),\text{ref}} = 100$ GPa, under $F_n = (350 \pm 25)$ nN applied normal load, the tip radius and contact radius were calculated from (1) and (2): $R_T = (52.6 \pm 1.3)$ nm and $a = (6.1 \pm 0.2)$ nm for no lateral contact coupling, and $R_T = (34.4 \pm 0.6)$ nm and $a = (5.2 \pm 0.2)$ nm for $k_{\text{lat}} = 0.75k_n$. The indentation modulus of the tip was taken as $M_T = 165$ GPa for Si(100) single crystal. We note that, for the same measured contact resonance frequencies on the Au(111) reference, the calculated tip radius differs according to the contact geometry considered: with or without lateral contact coupling. The two measured contact resonance frequencies on the Au(111) reference were also used to determine [11] that the tip was located at the end of the cantilever. In this case, we need to track only the first contact resonance frequency in order to calculate the contact stiffness on the investigated granular topography.

Although all the measurements were made in ambient humidity (relative humidity 40%), in our subsequent calculation we neglected the contribution of the water meniscus formed between the tip and the investigated surface and, consequently, described the elastic deformation of the contact by the Hertz model. This was motivated by the small values measured for the pull-off force between the tip and the surface at different locations across the sample: 10%–12%

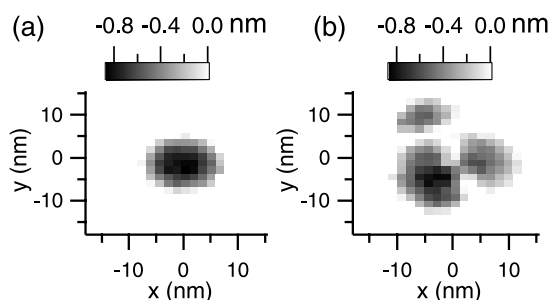


Figure 8. Tip-sample contact: (a) on top of the grains the contact is SAC; (b) within the intergrain regions a MAC is formed between the tip and the adjacent grains.

of the applied load. For such a small fraction, the humidity contribution is negligible to the measured contact resonance frequencies independent if the tip is either in SAC or MAC.

4. Data analysis

The effect of the contact area change on the measured contact resonance frequencies becomes essential in CR-AFM imaging when variations in the elastic modulus occur at the nanoscale. In this case we need to acknowledge any change in the contact geometry during scanning and consider this change in calculating the local elastic modulus. First, as the STM image is free of a tip dilation effect, the radii of curvature of the undeformed summits contacted by the tip at a given location in the scan were found by fitting the summits in figure 6(a) with spherical cap profiles. Second, the map of the contact stiffness, k_n , was calculated from the contact resonance frequency shown in figure 6(b) by using (14). Then, by overlapping the two images (topography and contact stiffness), the contact between the tip and the Au film was reconstructed pixel by pixel, with consideration of MAC formation as described by (15)–(18). For the involved image processing and analysis an Igor Pro (Wave Metrics) (see footnote 1) code was developed.

The normal load F_n was maintained constant in the measurements made on both the flat-surface reference Au film and the granular Au film. In the contact reconstruction, at a given location, the compressions δ_i in (15) and (16) were increased in small increments while the nearest summits came gradually into contact with the probe. The limit was reached when the total load, distributed over the contacted summits, equaled the applied load $F_n = 350$ nN. The contact so formed can be either SAC or MAC. The compressions δ_i were then used to calculate the contact area and the local average of the reduced elastic modulus. Under the same applied load, figure 8 shows the summit interception at the contact on top of a grain and within an intergrain region where three adjacent grains are in contact with the tip. The calculations were made for a tip radius $R_T = 34.4$ nm to consider a lateral contact coupling characterized by $k_{lat}/k_n = 0.75$. As can be seen in figure 8, on top of the grain there is a SAC characterized by a circular contact area, whereas within the intergrain region the contact area is defined by three adjacent circles. In our calculations we have neglected the overlap of the asperities forming a MAC and treated them as individual contacts. The contact area in MAC, figure 8(b), is larger than in SAC, and this increase determines the observed enhancement in the contact resonance frequency when the tip is located between grains. This change in the contact area has to be considered in calculating the elastic modulus from the measured contact stiffness on granular surfaces.

With the contact reconstruction as described above, in figure 9 are shown the calculated maps for the contact area and the indentation modulus over the scanned area. Qualitatively, grain delimitation is easily observed in both images and very good correlations with the topography and contact resonance frequency scans are identified. With the self-consistent consideration of the elastic properties of contacted surface, the MAC between tip and adjacent grains leads to an increase in the real contact area, as can be seen in figure 9(a). This increase in the contact area determines in turn a significant reduction of the calculated indentation modulus in the intergrain regions

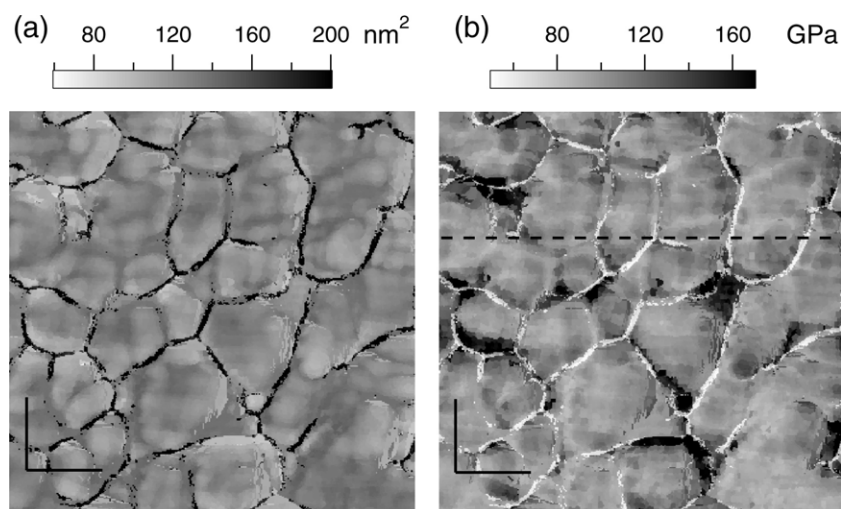


Figure 9. (a) Contact area and (b) indentation modulus maps calculated by correlating the STM topography and contact stiffness images. The scale bars are 100 nm.

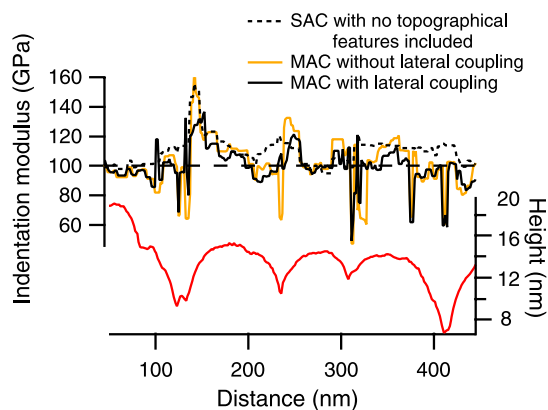


Figure 10. Topography (bottom) and calculated indentation modulus (top) along the dashed line shown in figure 9(b): dotted line with no topographical considerations, light line with MAC contributions but no lateral coupling, black line with MAC contributions and lateral coupling included.

(figure 9(b)). This pattern is consistently reproduced between close, well-round shaped grains that have an intergrain region of several nm. However, when the grain boundaries exhibit a ripple profile or the separation between adjacent grains is larger, the contact geometry deviates significant from the simple Hertzian model and the elastic modulus is erroneously calculated. Another source of error could come from the debris that infrequently become attached to the tip and possibly altered the measured contact resonance frequency by modifying the contact area. In this case the assumed geometry between the spherical tip and the STM topography deviates from the real contact geometry that contributes to CR-AFM measurements.

An intuitive variation of the elastic modulus along the grains is shown in figure 10 for the line profile marked with a dashed line in figure 9(b). All the profiles shown here are 2D cuts from 3D maps: topography (figure 6(b)) and elastic modulus maps (figure 9(b)) for MAC with lateral coupling and similar maps for SAC with no topographical features included and MAC without lateral coupling which are not shown here). Three different profiles were calculated for the indentation modulus along this line. The dotted one, with no consideration of any change in topography, correlates better with the measured contact resonance frequency and exhibits an unrealistic increase in the intergrain regions. In both cases when a MAC was considered, either with (black trace) or without (light trace) lateral coupling, a reduction of about 20% was calculated for the intergrain regions, in agreement with theoretical estimates [35]. However, a consistent reduction in the dispersion about the average value is observed in the line profile for the case when the lateral coupling is further included compared to the case with no lateral coupling. As is shown in figures 2 and 3, the reason is that the normal contact stiffness and, implicitly, the elastic modulus are overestimated when the lateral contact coupling exists but is not included in calculations.

In figure 11 are shown histograms of the indentation modulus values calculated over the whole scanned area for

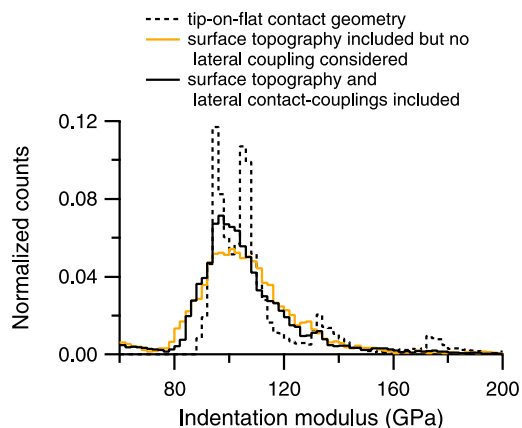


Figure 11. Histograms made of the calculated map of indentation modulus by considering the simple tip-on-flat contact geometry, and MAC geometry with and without lateral coupling corrections, respectively.

the three above-mentioned cases. In the first case, an invariant tip-on-flat contact geometry was assumed at every location in the scan. As can be seen, the histogram exhibits multiple peaks, inconsistent with the well-defined value of the elastic modulus for the (111) surface of Au single crystal. In the second (with no lateral contact coupling) and third (with lateral contact coupling) cases, the contact geometry was self-consistently calculated by correlating the topography and contact stiffness images. In these cases, the histograms approach bell shaped distributions around 100 GPa, the average value for the indentation modulus on Au(111) surfaces. Both histograms exhibit a tail at smaller values corresponding to the intergrain regions. As an improvement, the distribution for which the lateral contact coupling was included has a smaller width at half the maximum height compared with the case when the lateral contact coupling is ignored.

For the granular region as a whole, better correlations can be observed between the calculated map of the elastic modulus and the measured contact resonance frequency rather than with the topography. In topography, the grains look round and smooth but exhibit contrast in the contact resonance frequency. This is essentially due to the local change in the elasticity at the grain level and affects both the contact area and elastic modulus. Thus, even if on top of the grains the contact is essentially single-asperity, the contact area and elastic modulus are morphologically correlated and variations occur on every grain. In figure 9(b), the indentation modulus over the grains is calculated to be (100 ± 10) GPa, comparable to the value obtained from indentation on Au(111) surfaces [36]. Overall our measurements show a slightly softening in the elastic response of the Au grains (see figure 11) compared to the calculated indentation modulus for single-crystal Au(111), which is 100 GPa [24]. Similarly, but at the microscale, local elastic softening of metallic grains has been recently measured on polycrystalline copper by resonance ultrasound microscopy [10].

5. Conclusions

In this work we have considered the effect of topography in extracting the indentation modulus from CR-AFM measurements on granular Au films. Both topography and contact stiffness maps were self-consistently correlated to reveal nanoscale variations of the indentation modulus at the grain level. Consideration of the formation of multiple-asperity contacts between the AFM probe and the contacted grains provides realistic values for elastic modulus calculated from CR-AFM measurements. By taking into account the lateral contact coupling, besides the normal contact stiffness, an improvement in the measured indentation modulus has been shown. The analysis can be extended to other nanoscale structured materials where consideration of topography-induced artifacts is necessary.

Acknowledgments

We gratefully thank Dan Josell (NIST, Metallurgy Division) for Au films fabrication and Mark Vaudin (NIST, Ceramics Division) for x-ray analysis.

References

- [1] Craighead H G 2000 *Science* **290** 1532
- [2] Poncharal P, Wang Z L, Ugarte D and de Heer W A 1999 *Science* **283** 1513
- [3] Stan G, Ciobanu C V, Parthangal P M and Cook R F 2007 *Nano Lett.* **7** 3691
- [4] Gilbert B, Huang F, Zhang H, Waychunas G A and Banfield J F 2004 *Science* **305** 651
- [5] Gleiter H 2000 *Acta Mater.* **48** 1
- [6] Haque M A and Saif M T A 2004 *Proc. Natl Acad. Sci. USA* **101** 6335
- [7] Maivald P, Butt H J, Gould S A C, Prater C B, Drake B, Gurley J A, Elings V B and Hansma P K 1991 *Nanotechnology* **2** 103
- [8] Kolosov O V, Castell M R, Marsh C D, Briggs G A D, Kamins T I and Williams R S 1998 *Phys. Rev. Lett.* **81** 1046
- [9] Syed Asif S A, Wahl K J, Colton R J and Warren O L 2001 *J. Appl. Phys.* **90** 1192
- [10] Ogi H, Hiaro M, Tada T and Tian J 2006 *Phys. Rev. B* **73** 174107
- [11] Rabe U, Janser K and Arnold W 1996 *Rev. Sci. Instrum.* **67** 3281
- [12] Yamanaka K and Nakano S 1996 *Japan. J. Appl. Phys.* **35** 3787
- [13] Kolosov O and Yamanaka K 1993 *Japan. J. Appl. Phys.* **32** L1095
- [14] Cuberes M T, Assender H E, Briggs G A D and Kolosov O V 2000 *J. Phys. D: Appl. Phys.* **33** 2347
- [15] Drobek T, Stark R W and Heckl W M 2001 *Phys. Rev. B* **64** 045401
- [16] Cantrell S A, Cantrell J H and Lillehei P T 2007 *J. Appl. Phys.* **101** 114324
- [17] Yamanaka K, Maruyama Y, Tsuji T and Nakamoto K 2001 *Appl. Phys. Lett.* **78** 1939
- [18] Rabe U, Kopycinska M, Hinsekorn S, Munoz Saldana J, Schneider G A and Arnold W 2002 *J. Phys. D: Appl. Phys.* **35** 2621
- [19] Hurley D C, Kopycinska-Muller M, Koss A B and Geiss R H 2005 *Meas. Sci. Technol.* **16** 2167
- [20] Stan G and Price W 2006 *Rev. Sci. Instrum.* **77** 103707
- [21] Passeri D, Bettucci A, Germano M, Rossi M, Alippi A, Sessa V, Fiori A, Tamburri E and Terranova M L 2006 *Appl. Phys. Lett.* **88** 121910
- [22] Rabe U 2006 *Applied Scanning Probe Microscopy* vol II, ed B Bhushan and H Fuchs (Berlin: Springer) pp 37–90
- [23] Johnson K L 1985 *Contact Mechanics* (Cambridge: Cambridge University Press)
- [24] Vlassak J J and Nix W D 1993 *Phil. Mag. A* **67** 1045
- [25] Mindlin R D 1949 *J. Appl. Mech.* **16** 269
- [26] Hurley D C and Turner J A 2007 *J. Appl. Phys.* **102** 033509
- [27] Mazeran P E and Loubet J L 1997 *Tribol. Lett.* **3** 125
- [28] Weaver W Jr, Timoshenko S P and Young D H 1990 *Vibrational Problems in Engineering* 5th edn (New York: Wiley)
- [29] Dupas E, Gremaud G, Kulik A and Loubet J-L 2001 *Rev. Sci. Instrum.* **72** 3891
- [30] Rabe U, Amelio S, Kopycinska M, Hirsekorn S, Kemf M, Gorken M and Arnold W 2002 *Surf. Interface Anal.* **33** 65
- [31] Hutter J L and Bechhoefer J 1993 *Rev. Sci. Instrum.* **64** 1868
- [32] Palumbo G, Thorpe S J and Aust K T 1990 *Scr. Metall. Mater.* **24** 1347
- [33] Muthaswami L, Zheng Y, Vajtai R, Shehkawat G, Ajayan P and Geer R E 2007 *Nano Lett.* **7** 3891
- [34] Muraoka M 2005 *Nanotechnology* **16** 542
- [35] Wang G-F, Feng X-Q, Yu S-W and Nan C-W 2003 *Mater. Sci. Eng. A* **363** 1
- [36] Kiely J D and Houston J E 1998 *Phys. Rev. B* **57** 12588